coatings

MDPI

Article

Influence of Solid Waste Material Content on the Properties of Steel Slag-Waste Clay Brick Ceramic Bricks

Ying Ji [1,*,†], Enyao Li [1,†], Gang Zhu [2], Ruiqi Wang [1] and Qianqian Sha [1]

[1] College of Materials Science and Engineering, Xi'an University of Architecture and Technology, Xi'an 710055, China; lienyao@xauat.edu.cn (E.L.); 13363941368@163.com (R.W.); shaqianqian@xauat.edu.cn (Q.S.)
[2] China Building Materials Industry Construction Xi'an Engineering Co., Ltd., Xi'an 710065, China; cbmxe2023@163.com
* Correspondence: jiying@xauat.edu.cn
† These authors contributed equally to this work.

Abstract: Steel slag and waste clay brick are two common solid wastes in industrial production, and their complex chemical compositions pose challenges to the production of traditional alumina silicate ceramics. To investigate the influence of steel slag and waste clay brick on the performance of $CaO–SiO_2–MgO$ ceramic materials, this study examined their effects on the mechanical properties, crystal composition, and microstructure of the ceramics through single-factor experiments. The results demonstrate that when keeping the dosage of waste clay brick and talcum powder constant, a 43% dosage of steel slag yields optimal performance for the ceramic materials with a modulus of rupture of 73.01 MPa and a water absorption rate as low as 0.037%. Similarly, when maintaining a constant dosage of steel slag and talcum powder, a 41% dosage of waste clay brick leads to superior performance of the ceramic materials, with a modulus of rupture reaching 82.17 MPa and a water absorption rate only at 0.071%. Furthermore, when keeping the dosage of steel slag and waste clay brick constant, employing a talcum powder dosage of 24% results in excellent performance for the ceramic materials with a modulus of rupture measuring 73.01 MPa while maintaining an extremely low water absorption rate at only 0.037%. It is noteworthy that steel slag contributes to akermanite phase formation while talcum powder and waste clay brick contribute to diopside phase formation.

Keywords: ceramic tiles; steel slag; waste clay bricks; solid waste resource utilization

Citation: Ji, Y.; Li, E.; Zhu, G.; Wang, R.; Sha, Q. Influence of Solid Waste Material Content on the Properties of Steel Slag-Waste Clay Brick Ceramic Bricks. *Coatings* **2024**, *14*, 434. https://doi.org/10.3390/coatings14040434

Academic Editor: Csaba Balázsi

Received: 19 March 2024
Revised: 2 April 2024
Accepted: 3 April 2024
Published: 5 April 2024

1. Introduction

Ceramic tiles are widely used as building materials for indoor and outdoor wall and floor decoration, offering a wide range of options and having a rich historical background. The primary components include natural minerals such as clay, quartz, and feldspar, which undergo various processes including mixing, molding, drying, glazing, and high-temperature firing. The production of ceramic tiles heavily depends on the availability of high-quality mineral resources. However, in recent years, the depletion of these resources has led to an increasing rise in production costs for ceramics. As a result, many ceramic manufacturers actively seek new raw materials and production techniques to reduce expenses while preserving limited resource supplies. In this regard, some scholars have initiated investigations into using solid waste as alternative raw materials in ceramic manufacturing [1]. This approach not only effectively addresses waste disposal concerns but also significantly reduces raw material costs with notable environmental implications.

Steel slag (SS) is a significant byproduct generated in large quantities during the steel-making process, accounting for approximately 15%–20% of the total crude steel output [2]. In China, SS production reaches around 120 million tons annually; however, its utilization rate remains below 20% [3]. As a low-value-added material, a substantial amount of SS cannot be effectively processed and is often stockpiled outdoors. This not only occupies valuable land resources but also poses potential risks of land pollution and ecological

degradation in the surrounding areas [4]. In recent years, there has been increasing research interest in exploring resource utilization options for SS. Current approaches primarily focus on utilizing its high strength and wear resistance as road backfill material [5,6], leveraging its porosity and alkalinity for sewage treatment purposes [7,8], harnessing its rich P, Ca, and Si elements to produce fertilizer [9,10], or incorporating it as a component in cement mixers to manufacture cement products [11]. However, these utilization methods still face certain challenges. For instance, when using SS as raw materials for fertilizer production, the presence of MnO and other heavy metal elements may impact product safety.

Similarly, employing SS in the cement industry can lead to poor stability due to free CaO and MgO content within SS [12,13], making it difficult for large-scale usage. Recent studies have discovered that the main components of SS include CaO, SiO_2, Al_2O_3, MgO, and Fe_2O_3 along with clay, feldspar, and quartz—all traditional building ceramic raw materials with potential application prospects. Ceramic samples prepared from these constituents exhibit promising performance characteristics [14]. Some investigations have explored how variations in raw material composition influence the properties of ceramic brick samples made from SS. Tabit [15] investigated the impact of the CaO/SiO_2 ratio (0.12–0.8) on phase transformation in ceramic materials by adding SS to fly ash within a range of 10–50 wt. %. The findings revealed that plagioclase was the primary phase when the CaO/SiO_2 ratio ranged from 0.12 to 0.56, while at a ratio of 0.8, hornblende content significantly increased. Ai [16] and colleagues designed various ceramics with different SS ratios (0–70 wt. %) and used FACTsage 8.0 software to simulate phase formation processes. The simulation results indicated mullite formation within an SS content range of 0 to 25 wt. %, with plagioclase becoming the dominant crystalline phase between an SS content range of 25 wt. % to 45 wt. %, and hornblende production surpassing plagioclase production when the slag-to-binder ratio exceeded 45 wt. %. Zhang [17] discovered that reducing the MgO/Al_2O_3 ratio resulted in a transition from quartz and hornblende phases to quartz and plagioclase phases as primary crystalline phases; in contrast, high MgO content promoted hornblende formation, whereas high Al_2O_3 content favored plagioclase formation.

Clay brick, as a common building material, was widely used in various buildings in the early 20th century. However, with the development of the construction industry in various countries, brick concrete buildings have gradually been replaced by reinforced concrete buildings, leading to a significant increase in the amount of construction waste generated by demolition [18]. Among this, waste clay brick (WCB) accounts for about 50% of the total construction waste [18]. Unfortunately, due to the lack of effective mechanisms and means, less than half of this construction waste is recycled. As a result, a large number of difficult-to-treat waste clay bricks can only be continuously stacked. This not only occupies a substantial amount of land resources but also pollutes the surrounding soil and water [19,20]. Currently, research on recycling waste clay bricks mainly focuses on preparing recycled aggregates and conducting cement mixture tests [21–24]. However, using waste clay bricks as concrete aggregate reduces mixability and significantly weakens concrete products' strength [19,20,25–28].

Additionally, when used as a cement mixture, volcanic ash effect is limited due to low amorphous mineral content in waste clay bricks [29]. These problems further restrict large-scale comprehensive utilization. In recent years, global ceramic tile production and consumption have rapidly recovered from downturns. With increased production capacity comes an inevitable shortage problem for high-quality mineral resources such as clay quartz feldspar quartz sand, etc., which are consumed by the building ceramics industry [30]. The main mineral composition of discarded clay bricks consists of quartz and sodium feldspar, which is similar to the composition of raw materials used in ceramic tile production. Therefore, discarded clay bricks can be considered as a substitute for clay and feldspar in the production of ceramic tiles, providing a new approach to the resource utilization of discarded clay bricks. However, there is currently limited research on this topic; thus, further exploration is needed.

In this study, ceramic tiles were fabricated with varying compositions by adjusting the proportions of SS, waste clay bricks, and talc. The impact of raw material ratios on crystallization behavior, microstructure, and key mechanical properties was systematically investigated. The relative content of each crystal phase in the ceramic materials was determined using the XRD powder diffraction Rietveld refinement method, and the influence of different raw materials on the distribution of crystal phases in ceramic tiles was thoroughly discussed.

2. Materials and Methods

2.1. Materials

The raw materials used in this study include converter SS (manufactured by the Longgang Group, located in Xi'an, China.), waste clay bricks (manufactured by the Qingcaigou Construction Waste Disposal Plant, located in Xi'an, China.), and talcum powder (manufactured by the Guiguang Talcum Development Co., Ltd. located in Guilin, China).

Due to the high iron content present in SS, which may lead to the degradation of ceramic samples and restrict their usage, it is necessary to pretreat SS. The specific procedure involves crushing SS using a jaw crusher until it reaches a size of 1–2 cm, followed by the removal of iron scraps and Fe_3O_4 components using a strong magnet. After preliminary iron removal, the crushed SS is ground for 2 h in a φ500 mm × 500 mm ball mill rotating at a speed of 48 rev/min before being sieved through a 75 μm sieve and transferred into an anhydrous ethanol-filled beaker. Subsequently, the mixture is placed on a magnetic stirrer with a stirring speed set at 15–20 rev/s. Owing to variations in density and specific susceptibility among different phases within SS, mineral phases with low density and weak magnetic properties are suspended in the upper layer of ethanol solution while those with high density and strong magnetic properties settle at the bottom layer. The solid–liquid mixture obtained from both layers is filtered, dried at an oven temperature of 105 °C, and used accordingly. Other raw materials are also ground to achieve particle sizes of 75 μm using a ball mill before undergoing a drying process at an oven temperature of 105 °C for subsequent use. X-ray fluorescence analysis is employed to determine the chemical compositions of all three raw materials as presented in Table 1, where results are listed as oxides formulating their composition ratios. Additionally, the X-ray diffraction technique determines main phase compositions, as illustrated in Figures 1–3.

The steel slag consisted of several elements, including CaO, Fe_2O_3, SiO_2, MgO, and Al_2O_3, and it had a complex physical composition. Its crystal phase composition, in addition to dicalcium silicate and tricalcium silicate, also included other substances, such as magnetite and brownmillerite. The waste clay brick powder contained SiO_2, Al_2O_3, Fe_2O_3, CaO, MgO, Na_2O, K_2O, and TiO_2, as well as other alkali metal oxides. Its crystal phase composition was simpler, as it was primarily composed of quartz and andesine. Waste clay bricks can replace clay and feldspar as raw materials for ceramics. The chemical composition of talcum powder primarily includes SiO_2 and MgO, with the crystal phase composition exclusively limited to the talc phase. The relative composition of crystalline phases in the three raw materials can be observed in Table 2.

Table 1. Chemical composition of raw materials (wt. %).

	SiO_2	Al_2O_3	Fe_2O_3	MgO	CaO	Na_2O	K_2O	MnO	P_2O_5	TiO_2	Loss
SS	14.53	3.40	20.49	5.41	34.92	0.21	0.07	6.00	1.98	1.39	1.3
WCB	47.03	12.97	5.72	2.32	8.78	1.61	2.27	0.13	0.19	0.72	2.1
Talc	64.07	0.55	0.08	31.7	0.32	-	-	-	-	-	4.8

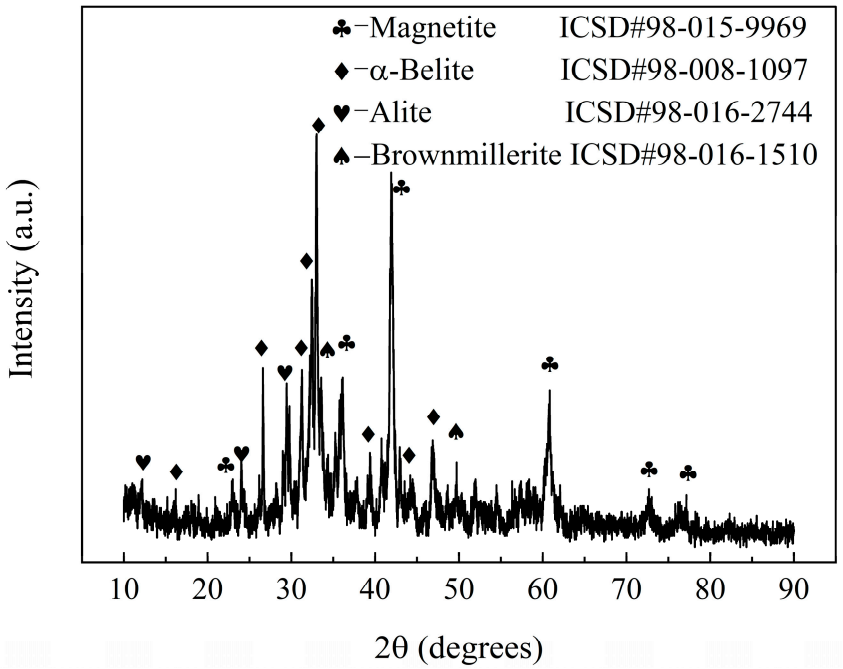

Figure 1. XRD pattern of SS.

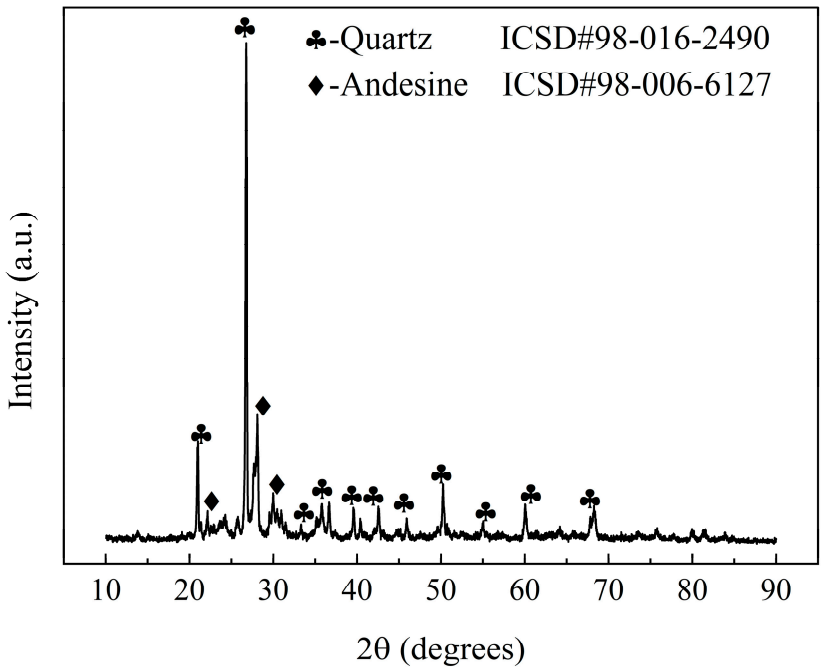

Figure 2. XRD pattern of WCB.

Table 2. Relative crystal phase content of raw materials.

	Magnetite (Fe_3O_4)	Alite ($3CaO{\cdot}SiO_2$)	Dicalcium Silicate–Alpha ($2CaO{\cdot}SiO_2$)	Brownmillerite ($4CaO{\cdot}Al_2O_3{\cdot}Fe_2O_3$)	Quartz (SiO_2)	Andesine ($(Na,Ca)[(Si,Al)_4O_8]$)	Talc ($Mg_3[Si_4O_{10}](OH)_2$)
SS	7.8	17.2	46.1	17.2	-	-	-
WCB	-	-	-	-	66.9	33.1	-
Talc	-	-	-	-	-	-	100

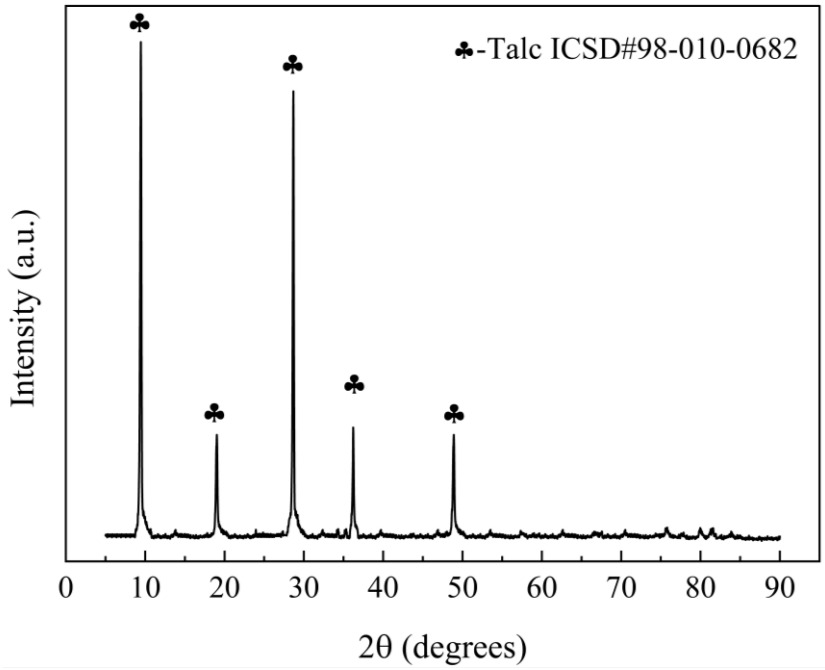

Figure 3. XRD pattern of Talc.

The particle size distributions of the three materials are illustrated in Figures 4–6, respectively. The SS powder exhibits D50 and D90 values of 11.80 μm and 45.49 μm, while the WCB demonstrates corresponding D50 and D90 values of 11.72 μm and 48.86 μm. In contrast, the talc powder displays a more homogeneous distribution with D50 and D90 values of 13.73 μm and 36.33 μm, respectively.

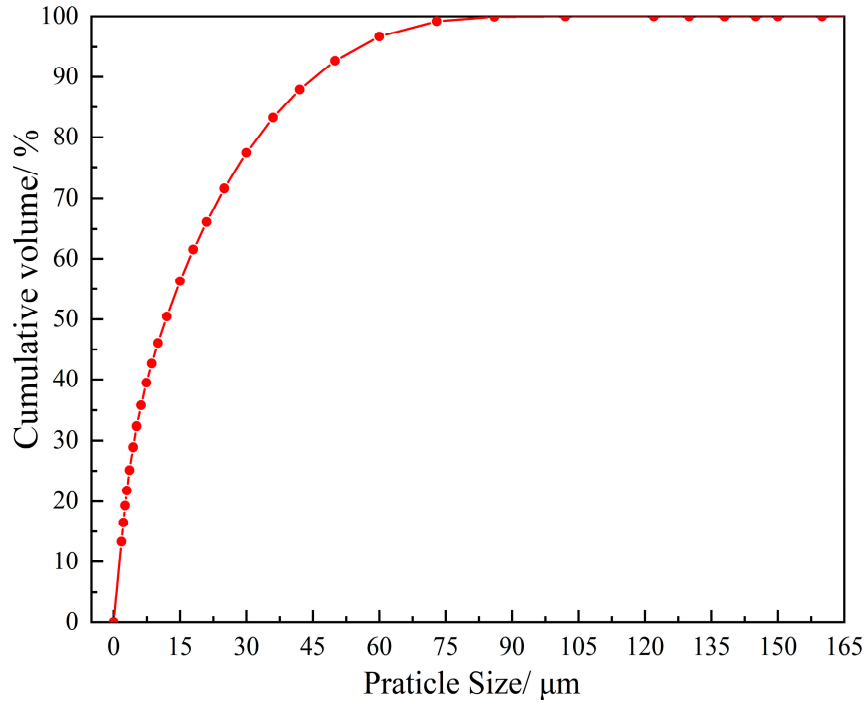

Figure 4. Particle size distribution of SS.

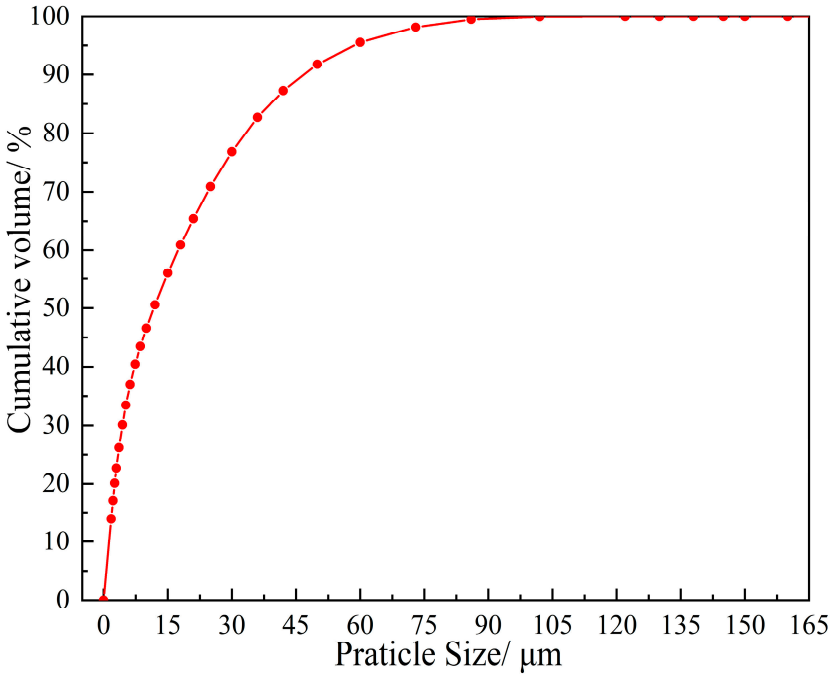

Figure 5. Particle size distribution of WCB.

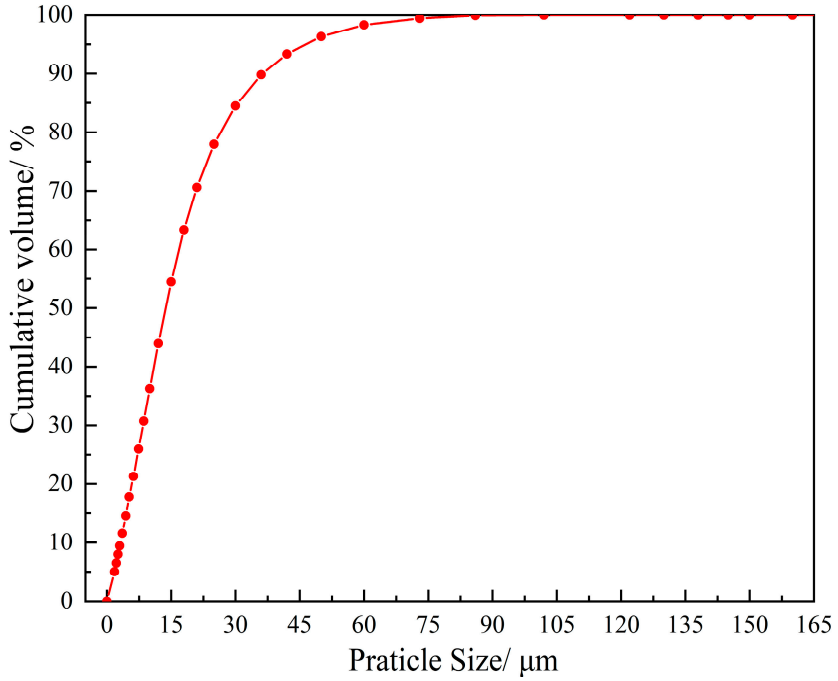

Figure 6. Particle size distribution of talc.

The SEM images of the three raw material powders are presented in Figures 7–9. These figures clearly show that both SS and WCB powder particles have irregular shapes and non-uniform sizes, whereas talc powder consists of relatively uniform flaky particles. In Figure 7d, there are hexagonal plate-like crystal phases indicating tricalcium silicate in the SS powder; round granular crystal phases representing dicalcium silicate are also present; brown millerite phase fills the calcium–silicon phases continuously; white particles with both round and amorphous structures represent the magnetite phase. In Figure 8d, hexagonal columnar crystals indicate a quartz phase, while block crystals represent an andesine phase. Finally, in Figure 9d, flaky crystals corresponding to the talc phase can be seen.

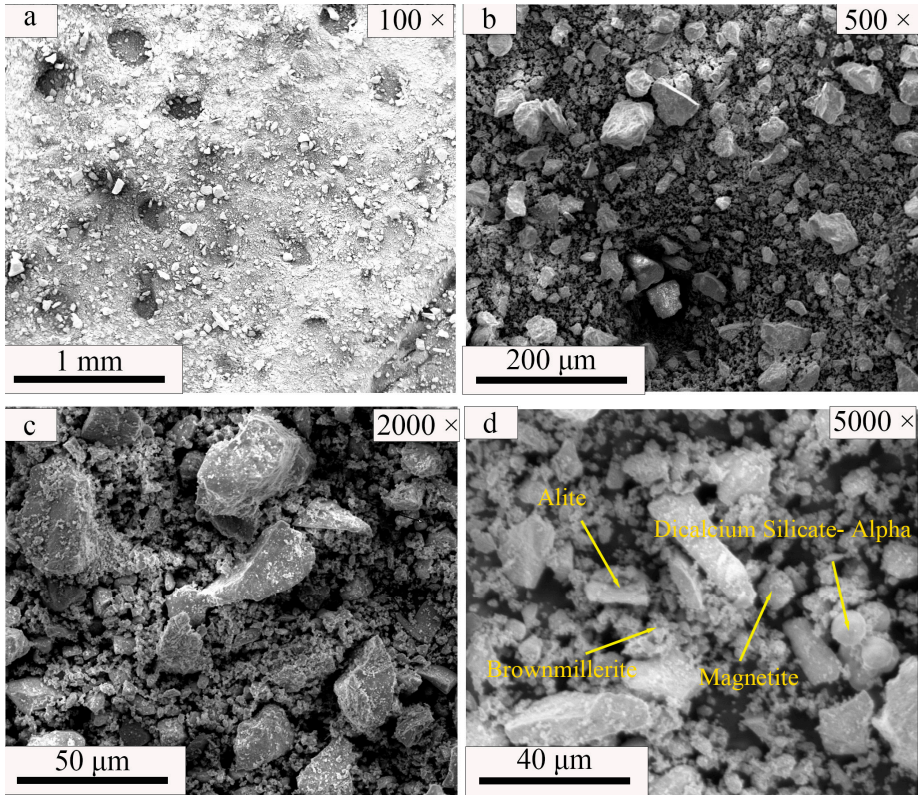

Figure 7. SEM images of SS powders at different magnifications: (**a**) 100× SEM image, (**b**) 500× SEM image, (**c**) 2000× SEM image, (**d**) 5000× SEM.

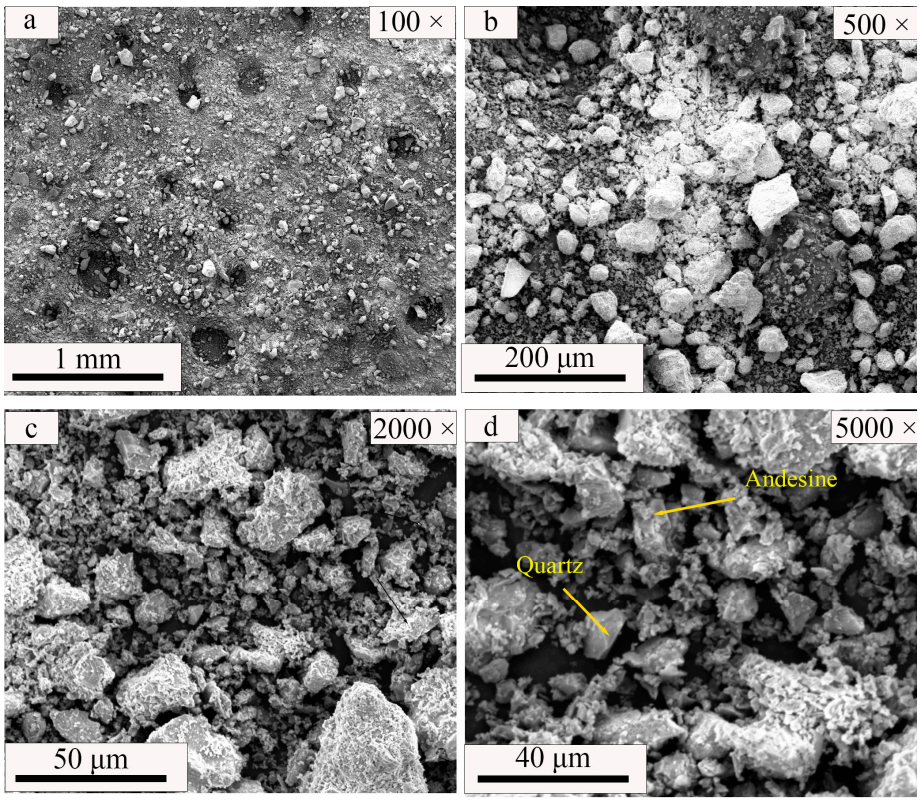

Figure 8. SEM images of WCB powders at different magnifications: (**a**) 100× SEM image, (**b**) 500× SEM image, (**c**) 2000× SEM image, (**d**) 5000× SEM.

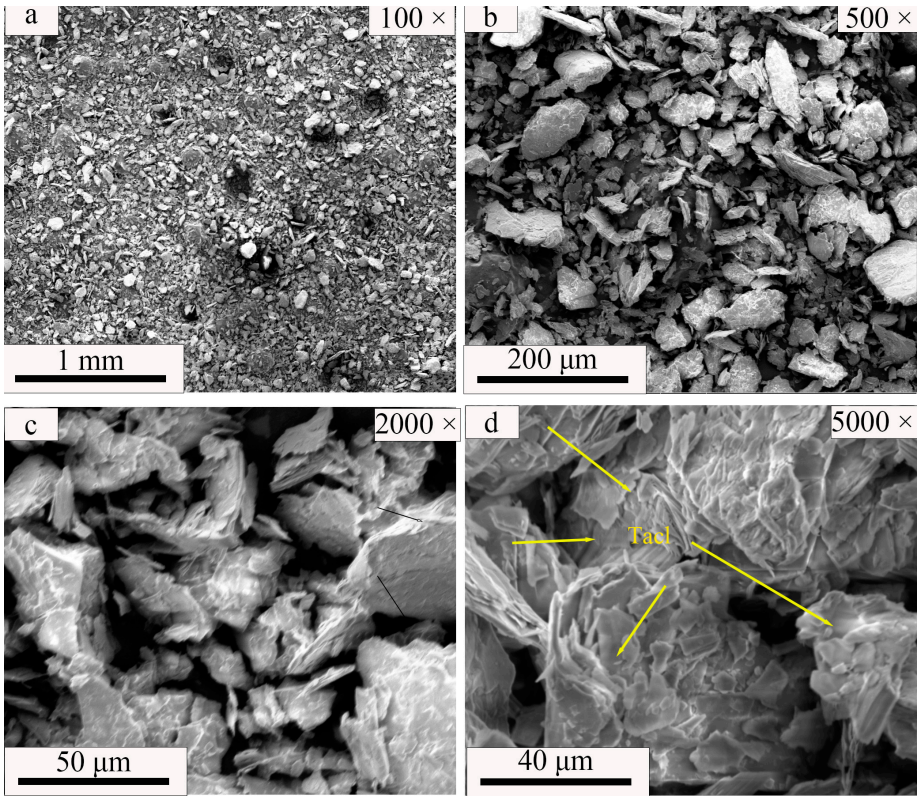

Figure 9. SEM images of talc powders at different magnifications. (**a**) 100× SEM image, (**b**) 500× SEM image, (**c**) 2000× SEM image, (**d**) 5000× SEM.

2.2. Formula Design

In this experiment, the influence of varying dosages of SS, WCB, talc, and three other raw materials on the performance of ceramic tiles was investigated as the individual factor. The specific formulations are presented in Tables 3–5 (providing mass ratios and percentages). Tables 6–8 display the chemical composition derived from calculations based on Table 1 along with Tables 3–5.

Table 3. Ceramic tile formulations with different SS content.

	SS		WCB		Talc	
YG-1	30 g	33%	35 g	39%	25 g	28%
YG-2	35 g	37%	35 g	37%	25 g	26%
YG-3	40 g	40%	35 g	35%	25 g	25%
YG-4	45 g	43%	35 g	33%	25 g	24%
YG-5	50 g	45%	35 g	32%	25 g	23%

Table 4. Ceramic tile formulations with different WCB content.

	SS		WCB		Talc	
YZ-1	45 g	45%	30 g	30%	25 g	25%
YZ-2	45 g	43%	35 g	33%	25 g	24%
YZ-3	45 g	41%	40 g	36%	25 g	23%
YZ-4	45 g	39%	45 g	39%	25 g	22%
YZ-5	45 g	37.5%	50 g	42%	25 g	20.5%

Table 5. Ceramic tile formulations with different talc content.

	SS		WCB		Talc	
YH-1	45 g	45%	35 g	35%	20 g	20%
YH-2	45 g	43%	35 g	33%	25 g	24%
YH-3	45 g	41%	35 g	32%	30 g	27%
YH-4	45 g	39%	35 g	30%	35 g	31%
YH-5	45 g	37.5%	35 g	29.1%	40 g	33.3%

Table 6. Chemical composition of ceramic tile formula with different SS content (wt. %).

	SiO_2	Al_2O_3	Fe_2O_3	MgO	CaO	Na_2O	K_2O	MnO	P_2O_5	TiO_2
YG-1	41.72	6.34	9.02	11.88	15.04	0.70	0.91	2.03	0.73	0.74
YG-2	39.44	6.20	9.72	11.10	16.25	0.67	0.87	2.27	0.80	0.78
YG-3	38.29	6.04	10.22	10.90	17.12	0.65	0.82	2.45	0.86	0.81
YG-4	37.14	5.87	10.72	10.70	17.99	0.62	0.78	2.62	0.91	0.84
YG-5	36.96	5.81	11.07	10.78	18.60	0.61	0.76	2.74	0.95	0.86

Table 7. Chemical composition of ceramic tile formula with different WCB content (wt. %).

	SiO_2	Al_2O_3	Fe_2O_3	MgO	CaO	Na_2O	K_2O	MnO	P_2O_5	TiO_2
YZ-1	36.67	5.56	10.96	11.06	18.43	0.58	0.71	2.74	0.95	0.84
YZ-2	37.14	5.87	10.72	10.70	17.99	0.62	0.78	2.62	0.91	0.84
YZ-3	37.62	6.19	10.48	10.34	17.55	0.67	0.85	2.51	0.88	0.83
YZ-4	38.10	6.51	10.24	9.99	17.11	0.71	0.91	2.39	0.85	0.82
YZ-5	38.34	6.84	10.10	9.50	16.85	0.75	0.98	2.30	0.82	0.82

Table 8. Chemical composition of ceramic tile formula with different talc content (wt. %).

	SiO_2	Al_2O_3	Fe_2O_3	MgO	CaO	Na_2O	K_2O	MnO	P_2O_5	TiO_2
YH-1	35.81	6.18	11.24	9.59	18.85	0.66	0.83	2.75	0.96	0.88
YH-2	37.14	5.87	10.72	10.70	17.99	0.62	0.78	2.62	0.91	0.84
YH-3	38.31	5.69	10.25	11.52	17.21	0.60	0.76	2.50	0.87	0.80
YH-4	39.64	5.39	9.73	12.63	16.35	0.56	0.71	2.38	0.83	0.76
YH-5	40.38	5.34	9.43	13.03	15.83	0.56	0.71	2.29	0.80	0.74

2.3. Sample Preparation Methods

According to the formulated recipe, 500 g of raw materials is accurately weighed and mixed in a mixer for 60 min to ensure complete homogeneity. The uniformly mixed raw materials are then fed into a disc granulator with a set speed of 40 rev/min. Water is manually sprayed using a spray bottle, adding approximately 10% of the granulated material as water to achieve moisture content within the desired range of 7%–9%. The granulated material is then sieved, selecting particles ranging in size from 0.18 mm to 0.85 mm. These particles are sealed in bags and stored in a cool place for aging purposes for at least 24 h to allow sufficient internal moisture penetration and uniform distribution throughout the pellets. The aged pellets are poured into metal molds with dimensions of 50 × 50 mm and subjected to mechanical pressure until they form compacted billets with dimensions of 50 × 50 × 8 mm. The molding pressure is set at 25 MPa with an applied load rate of 0.5 KN/s. Subsequently, the samples are dried in an oven at 105 °C for 24 h, resulting in billets with certain strength. The dried billets are placed inside mullite saggers and fired in a high-temperature furnace reaching maximum firing temperature during this process of 1190 °C with a holding time of 60 min, to obtain ceramic tile samples.

2.4. Sample Performance Measurements

2.4.1. Macroscopic Performance Measurements

The fired samples underwent physical tests for water absorption and modulus of rupture (three-point bending strength). The water absorption rate was determined using the vacuum method specified in GB/T 3810.4-2016 *Test Methods for Ceramic Bricks* [31,32]. Equation (1) expresses the relationship between the water absorption rate (E), water absorption mass (m_2), and dry sample mass (m_1).

$$E = \frac{m_2 - m_1}{m_1} \times 100\% \quad (1)$$

The modulus of rupture is determined through testing using the three-point bending method. The sample is positioned on the flexural fixture, ensuring that the center rod maintains an equal distance between both support rods. A consistent load, applied at a rate of 1 N/(mm^2·s) $\pm$ 0.2 N/(mm^2·s), results in recording the fracture load F for a subsequent calculation of modulus of rupture R as per formula (2).

$$R = \frac{3Fl_2}{2bh^2} \quad (2)$$

where F is the fracture load in N; l_2 is the span between two supporting rods in mm; b is the width of the sample in mm; and h is the minimum thickness of the fracture surface of the sample measured along the fracture edge after the test in mm.

2.4.2. Microscopic Performance Measurements

We utilized a D/MAX 2000 X-ray diffractometer to determine the crystal phase composition of sintered samples. The target material is Cu, with a tube voltage of 40 kV, tube current of 26 mA, and power output of 1600 W. Scanning angles range from 10–90° with a step size set at 0.02 and scanning speed set at 5°/min. HighScore (Plus) 3.5 software is employed for Rietveld refinement analysis to determine the relative content of each phase in the sample. Quanta200 scanning electron microscopy is used to observe pore structure, densification degree, and crystal morphology as well as element distribution in the sintered samples. ImageJ image processing tool is utilized for the simple measurement of surface pore structure and crystal size within SEM images.

3. Results

3.1. Physical and Mechanical Properties

The influence of changes in SS content on the water absorption and modulus of rupture of ceramic samples is illustrated in Figure 10 while keeping the WCB and talc contents constant. It can be observed that as the SS content increases, the modulus of rupture of ceramic samples exhibits a decreasing trend, reaching its maximum value at 43% SS content with a value of 73.01 MPa. This suggests that increasing the SS content contributes to enhancing the densification degree of ceramic samples. When the SS content in the formulation is below 43%, there is a gradual decrease in water absorption rate with increasing SS content, reaching a minimum value of 0.04% at 43%. However, when the SS content reaches 45%, both water absorption rate and modulus of rupture sharply decline due to an abundance of metal oxide components producing a low-viscosity liquid phase during the sintering process, resulting in increased porosity and deterioration in mechanical properties for sintered samples. Furthermore, it should be noted that all groups of ceramic bricks prepared with an SS content ranging from 33% to 45% exhibit significantly superior properties compared to those specified by Chinese national standards [31,32], including a water absorption rate lower than 0.5% and a modulus of rupture greater than or equal to 35 MPa.

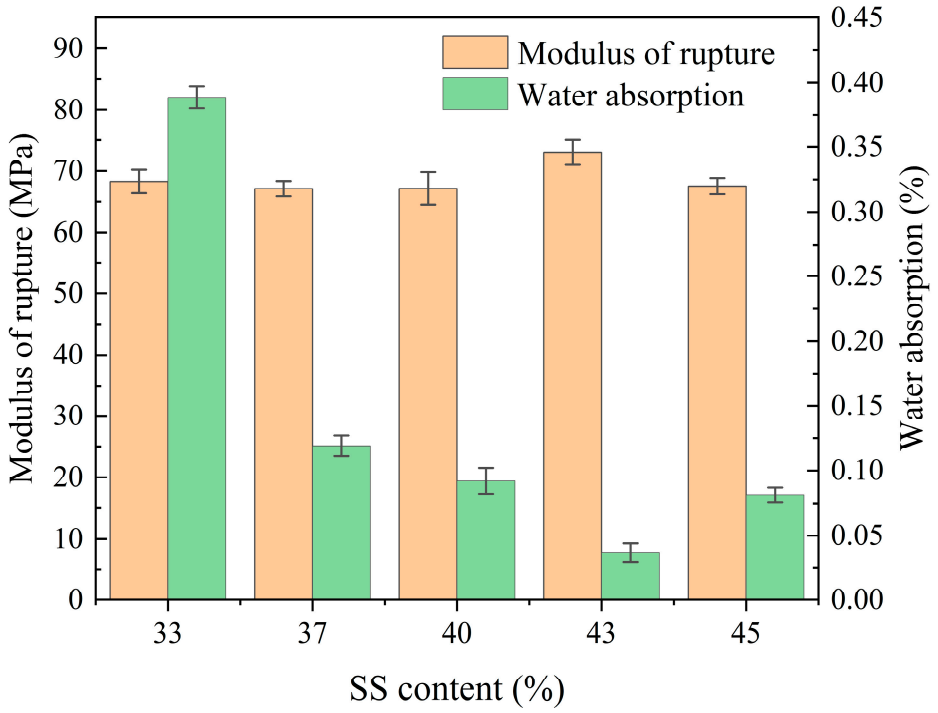

Figure 10. Water absorption and rupture modulus under different SS content.

The influence of WCB content change on water absorption and modulus of rupture of ceramic samples is illustrated in Figure 11 while keeping SS and talc content constant. It can be observed that the modulus of rupture initially increases and then decreases with increasing WCB content. The smallest modulus of rupture of the sample, 55.69 MPa, is achieved at a WCB content of 30%, whereas the maximum value of 82.17 MPa is obtained at a WCB content of 36%. Furthermore, as the WCB content increases, the water absorption of ceramic samples significantly decreases from 3.07% at 30% to 0.04% at 33%, followed by a slight increase; however, it remains consistently below 0.5%. Additionally, it should be noted that the mechanical properties of all groups prepared with WCB contents ranging from 30%–42% surpass those specified in Chinese national standards [31,32], which require a modulus of rupture greater than or equal to 35 MPa and water absorption less than or equal to 0.5%.

The influence of talc content on water absorption and modulus of rupture of ceramic samples is illustrated in Figure 12 while keeping SS and WCB content constant. Initially, an increase in talc content leads to a rise in modulus of rupture followed by a decline. The lowest value of modulus of rupture (26.97 MPa) is observed at 33.3% talc content, whereas the highest value (73.01 MPa) is obtained at 24%. Furthermore, there is an initial decrease followed by a significant increase in water absorption with increasing talc content. At 20% talc content, the water absorption is 0.106%, which reduces to 0.037% at 24%. However, when the talc content exceeds 27%, there is a sharp deterioration in ceramic tile performance as indicated by increased water absorption up to its maximum value of 12.31%. Additionally, all properties for each group of ceramic bricks prepared with talc contents between 20%–33.3% meet Chinese national standards [31,32] that require a modulus of rupture greater than or equal to 35 MPa and water absorption less than or equal to 0.5%.

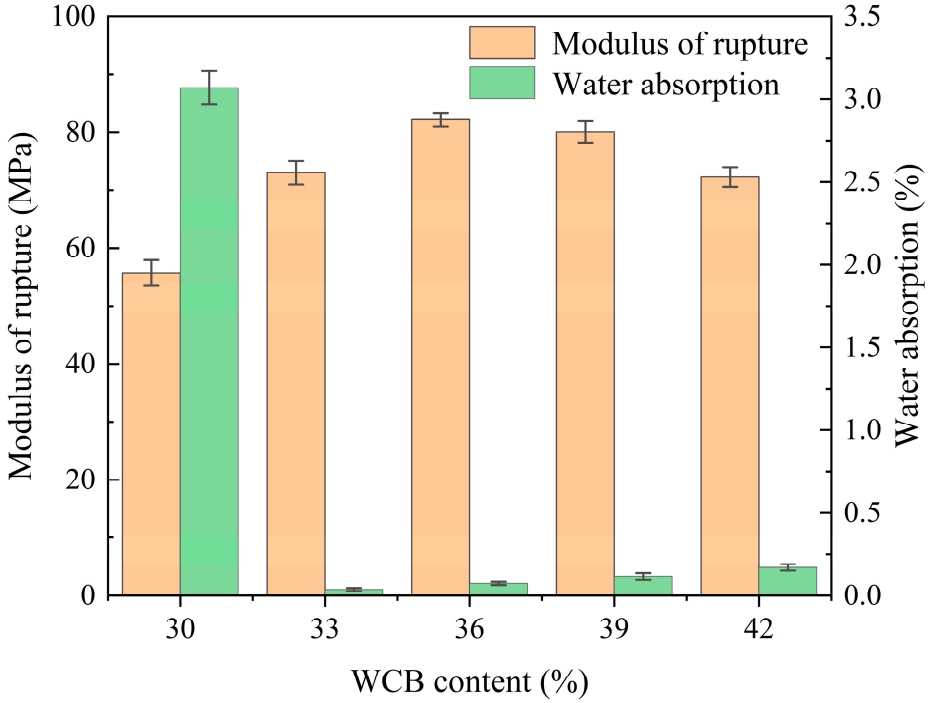

Figure 11. Water absorption and rupture modulus at different WCB content.

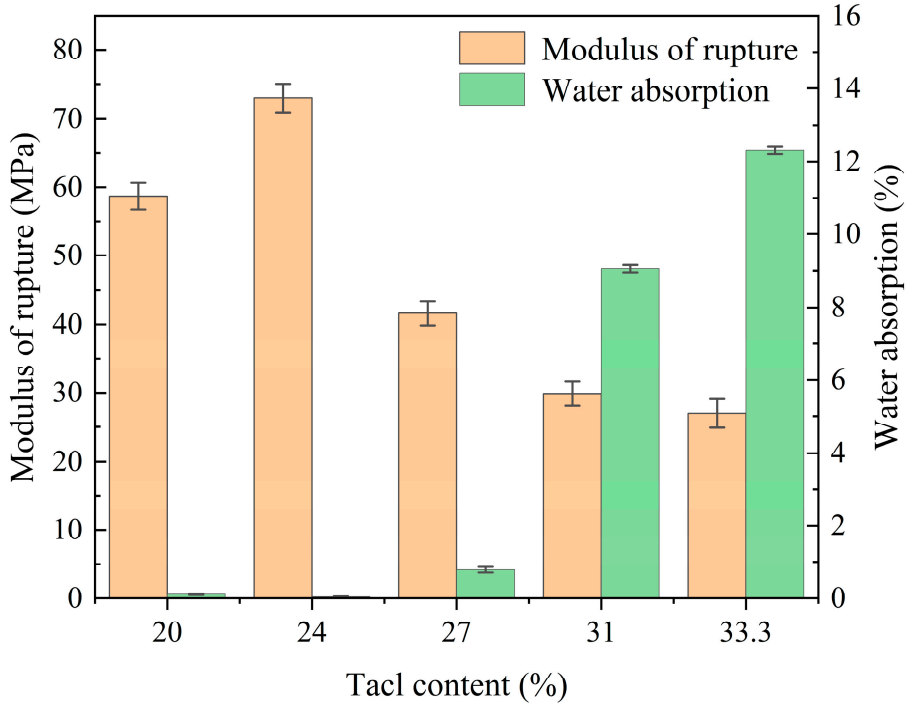

Figure 12. Water absorption and modulus of rupture under different talc content.

3.2. XRD Analysis

The crystal composition in the sample remained unchanged with the increase in SS content, as depicted in Figure 13. The identified crystal phases still included akermanite, diopside, and magnetite. The variation trend in the intensity of the main diffraction peaks for different crystal phases in samples prepared with varying SS contents is presented in Table 9 (akermanite, 2θ = 31.26; diopside, 2θ = 31.26; magnetite, 2θ = 62.08). Increasing the SS content leads to a continuous enhancement of the diffraction peaks corresponding to

akermanite and magnetite, while the diffraction peak associated with diopside consistently exhibits a weakening trend.

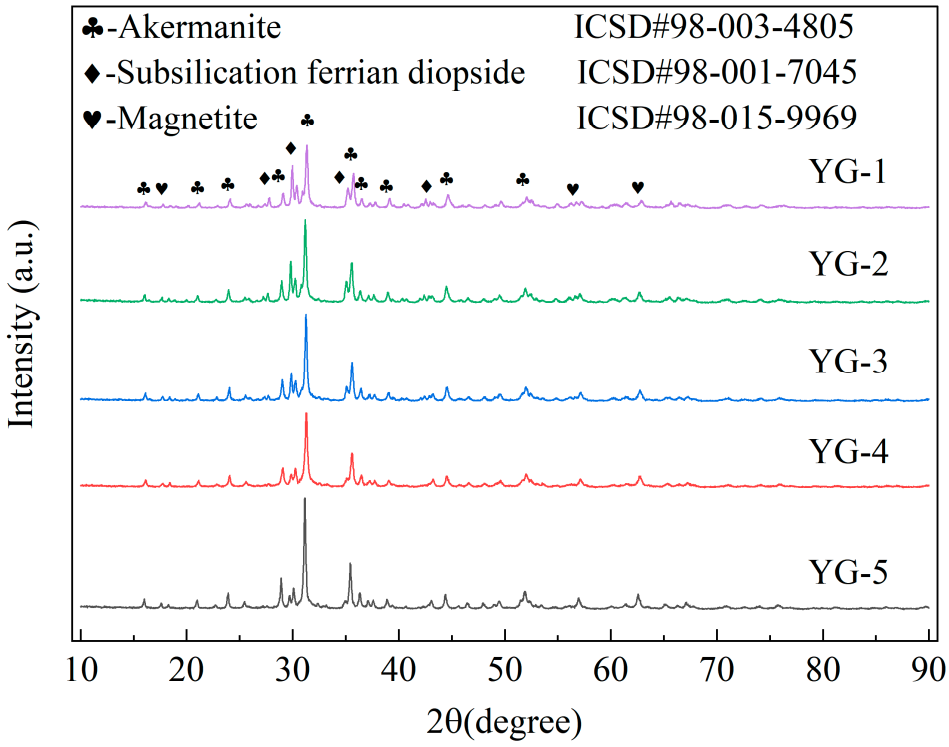

Figure 13. XRD pattern of samples with different SS content.

Table 9. Strength of main diffraction peaks of samples with different SS contents.

	Akermanite (I/Counts)	Diopside (I/Counts)	Magnetite (I/Counts)
YG-1	2008	1363.33	256.667
YG-2	2658.33	1318.33	336.667
YG-3	2761.71	900	382.33
YG-4	3204.17	783.33	401.22
YG-5	3508.33	401.22	446.67

After examining Figure 14, it can be inferred that the inclusion of WCB does not alter the crystal phases present in the sample. The primary constituents still comprise akermanite, diopside, and magnetite. The variation trend in the main diffraction peak intensity for each crystal phase in samples prepared with different WCB contents is presented in Table 10 (akermanite, 2θ = 31.26; diopside, 2θ = 31.26; magnetite, 2θ = 62.08). With an increasing WCB content, significant changes are observed in the diffraction peak intensities of each phase. Specifically, the diffraction peak intensities of akermanite and magnetite gradually decrease, while that of diopside continues to increase. At a WCB content of 39%, the difference in diffraction peak intensity between akermanite and diopside becomes indistinguishable; however, when the WCB content increases to 42%, the diffraction peak intensity of diopside surpasses that of akermanite.

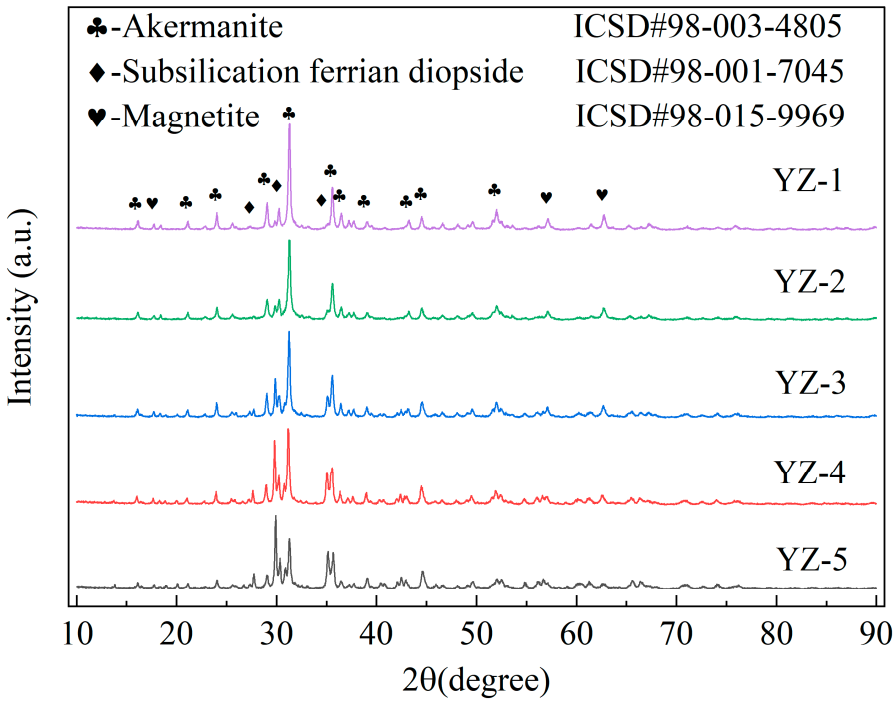

Figure 14. XRD pattern of samples with different WCB content.

Table 10. Strength of main diffraction peaks of samples with different WCB contents.

	Akermanite (I/Counts)	Diopside (I/Counts)	Magnetite (I/Counts)
YZ-1	3111.67	283.33	458.33
YZ-2	3204.17	783.33	401.22
YZ-3	2512.33	1148.33	328.33
YZ-4	2250	1908.33	293.33
YZ-5	1496.67	2161.67	180

The addition of talc content did not result in the formation of any new crystal phases in the sample, except for akermanite, diopside, and magnetite, as shown in Figure 15. The trends in the intensity of the main diffraction peaks for crystalline phases in samples prepared with varying talc contents are presented in Table 11 (akermanite, 2θ = 31.26; diopside, 2θ = 31.26; magnetite, 2θ = 62.08). However, significant changes were observed in the diffraction peak intensities of each phase as the talc content increased. Specifically, an increase in talc content resulted in a gradual decrease in relative abundance for the diopside phase while causing a continuous rise in diffraction peak intensity for the akermanite phase. At a talc content of approximately 31%, it became nearly impossible to observe any discernible peak intensity associated with the diopside phase. It is noteworthy that throughout this process, there was little change observed regarding magnetite crystal's diffraction peak intensity.

Table 11. Strength of main diffraction peaks of samples with different talc contents.

	Akermanite (I/Counts)	Diopside (I/Counts)	Magnetite (I/Counts)
YH-1	2728.33	973.33	361.66
YH-2	3204.17	783.33	401.22
YH-3	3426.67	908.33	456.66
YH-4	3491.67	166.67	156.667
YH-5	3521.43	156.667	446.67

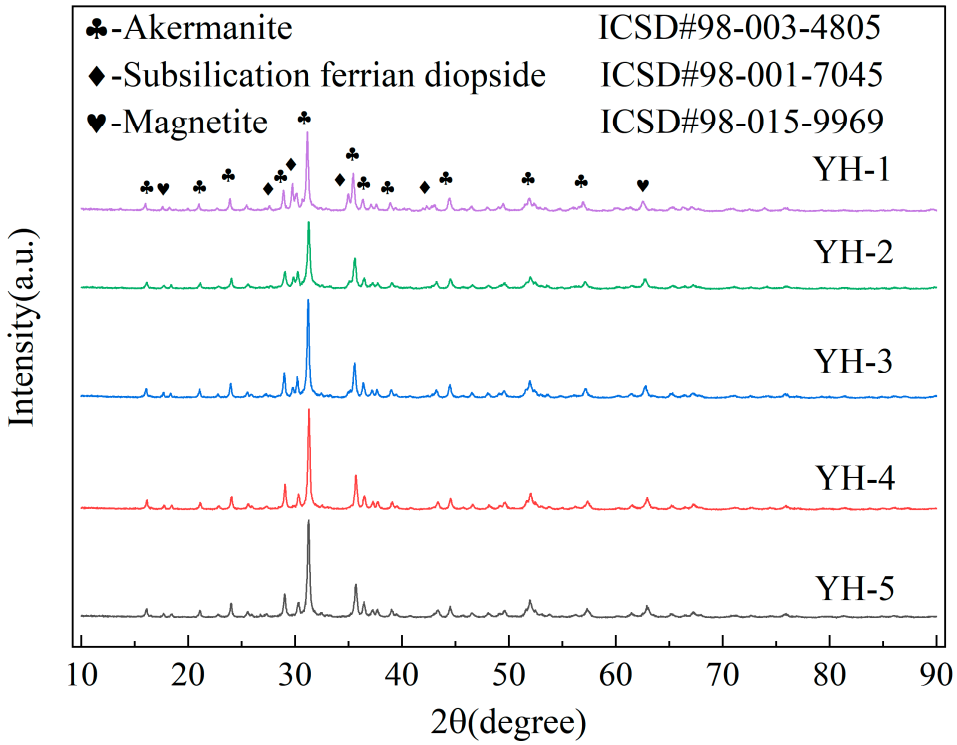

Figure 15. XRD pattern of samples with different talc content.

To further investigate the changes in crystalline phase content, we employed the XRD powder diffraction Rietveld refinement method to accurately determine the relative abundance of each crystalline phase present in the ceramic materials.

The relative proportions of crystal phases in samples with varying raw material dosages are displayed in Table 12. It is evident that there is a significant increase in the relative content of the akermanite phase in ceramic tile samples as the SS doping amount increases. Initially, the relative content of the akermanite phase was only 40.3%, but it surged to 75.7% with an increase in SS doping amount up to a certain extent, indicating that SS plays a crucial role in promoting the formation of the akermanite phase. Meanwhile, there is also a noticeable decrease in the relative content of diopside in ceramic tile samples, as its initial proportion was high at 53.1%. This proportion keeps decreasing and finally reaches 11.7% with an increase in SS doping amount. Additionally, during increasing concentration levels of SS doping, there is a fluctuating trend observed for magnetite's relative content, showing an initial proportion at 6.6%, gradually rising to reach 12.5%.

The relative content of the diopside phase within the ceramic tile sample shows an evident upward trend as the WCB content gradually increases. When the WCB content reaches 50%, there is a substantial increase in diopside phase content from its initial value of 8.2% to 72.9%. This finding emphasizes the essential role of WCB in facilitating diopside phase formation. Simultaneously, there is an evident decreasing trend observed in the relative content of the akermanite phase in ceramic tile samples. In the initial stage, the akermanite phase accounted for as high as 80% of the total phases present; however, with increasing WCB content, its proportion gradually decreased until it finally dropped to 27.1%. Additionally, we also noted a declining trend in the relative content of the magnetite phase during increases in WCB concentration. Initially, at 11.9%, its proportion gradually diminished with rising levels until no presence of magnetite could be detected when reaching a concentration level of 50%. With the increase in talcum powder content, there is a significant upward trend observed in the relative content of the akermanite phase within the ceramic samples. Initially, this phase accounts for only 64.5% of the composition. However, when the talcum powder content reaches 31%, its proportion rises significantly to 86.5% and remains unchanged thereafter, despite further increases

in talcum yield. Concurrently, there was a substantial decrease observed in the relative content of the diopside phase within the ceramic tile samples. Initially constituting as high as 25.3% of the composition, its content continued to decline with increasing talc content until it completely disappeared at a talc content of 31%. Furthermore, following the disappearance of diopside, a slight increase can be noted in the relative content of the magnetite phase within these ceramic samples. This phenomenon may be attributed to vacancies present within the diopside's lattice structure that are capable of accommodating metal ions [33]. Consequently, iron ions dissolve into diopside-forming magnetite crystals; however, without any remaining diopside crystals within these samples, iron ions that would have otherwise solid-dissolved exist instead as magnetite crystals, leading to an increased relative content.

Table 12. Relative crystal phase content.

	Akermanite (%) ($Ca_2MgSi_2O_7$)	**Diopside (%) ($CaMgSi_2O_6$)**	**Magnetite (%) (Fe_3O_4)**
YG-1	40.3	53.1	6.6
YG-2	56.5	35.3	8.3
YG-3	57.5	33.6	8.9
YG-4	67.4	21.3	11.3
YG-5	75.7	11.7	12.5
YZ-1	80	8.2	11.9
YZ-2	67.5	21.3	11.3
YZ-3	59.2	32	8.8
YZ-4	47.2	51.8	1.0
YH-1	64.5	25.3	10.2
YH-2	67.5	21.3	11.3
YH-3	77.1	12.1	10.8
YH-4	86.3	-	13.7

3.3. SEM Analysis

The EDS spectrum analysis diagram of the sample, as shown in Figure 16, reveals that the crystal morphology within the ceramic brick primarily consists of short columnar, plate-like, and rhombohedral structures. By combining XRD analysis with this observation, it becomes evident that the hexagonal-based columnar and plate-like crystals (labeled A and B, respectively) correspond to akermanite [34], while the irregular tetragonal-based columnar crystals (labeled C) correspond to diopside [17]. Furthermore, the rhombohedral structure corresponds to magnetite crystals (labeled D) [35]. Additionally, it is noteworthy that Si, Ca, and Mg are predominantly concentrated in both akermanite and diopside phases, whereas Fe is mainly distributed within the glass phase along with magnetite phases. Only a small amount of Fe solidly dissolves into the diopside phase. Lastly, Al is primarily distributed within the glass phase.

The SEM diagram in Figure 17 illustrates the surface morphology of the sample with varying SS content, magnified by a factor of 100. The shape and distribution of surface features change as SS content varies. At an SS content of 30%, numerous irregularly shaped pores with an average diameter of 56 μm and several larger holes exceeding 85 μm in diameter are observed on the sample surface. Upon increasing the SS content to 35%, pore distribution becomes more uniform, exhibiting rounder shapes, and is no longer concentrated in specific areas; furthermore, the average pore size decreases to 46.92 μm. With a further increase in SS content, both the number and size of pores on the sample surface progressively decrease. When reaching an SS content of 45%, the smallest average pore diameter within the sample is achieved (35.15 μm). However, at an SS content of 50%, large pores larger than 100 μm start appearing on the ceramic surface again, leading to a rise in average pore size (61.32 μm).

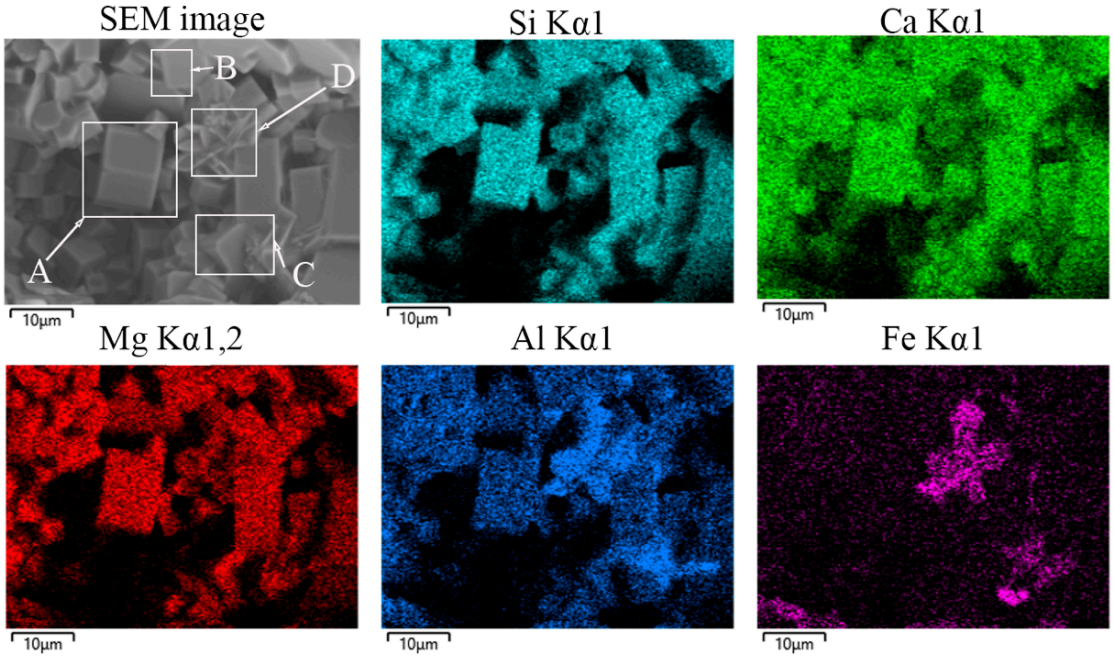

Figure 16. EDS diagram of ceramic tile sample (A and B correspond to akermanite, C indicates diopside, and D denotes magnetite).

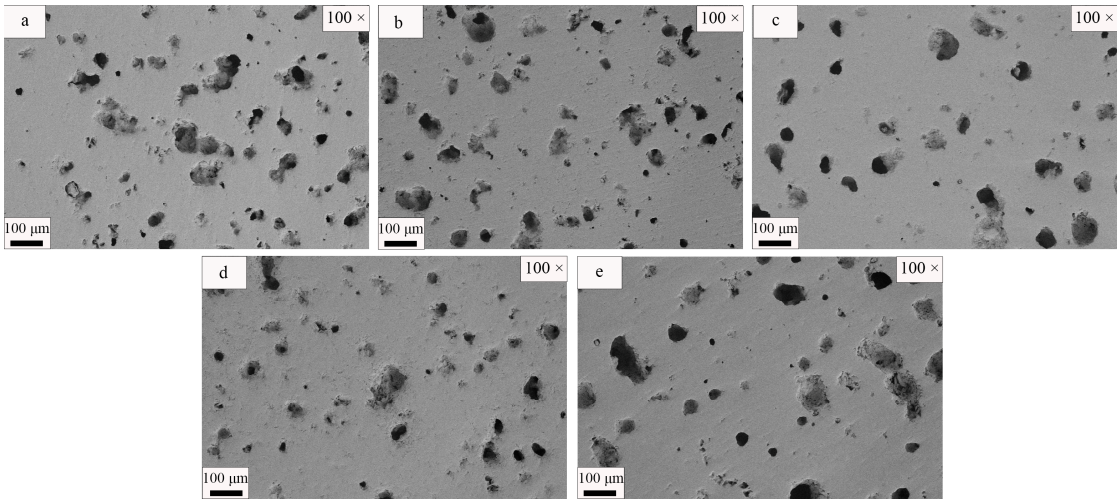

Figure 17. SEM images of samples at 100× magnification under different SS conditions: (**a**) YG-1; (**b**) YG-2; (**c**) YG-3; (**d**) YG-4; (**e**) YG-5.

The SEM images in Figure 18 depict samples with varying SS content, revealing corresponding changes in crystal type and density within the material. It is evident from the observations that an increase in SS content leads to a gradual rise in the number of columnar crystals, plate crystals, and rhombohedral crystals with hexagonal bottom surfaces, while the count of columnar crystals with irregular quadrilateral bottom surfaces decreases gradually. These findings align with those presented in Table 12, which indicate a progressive increase in relative contents of akermanite and magnetite phases alongside a decrease in diopside content. Furthermore, Figure 18 demonstrates that as SS content increases, there is a gradual enhancement in densification within the ceramic sintered billet. In Figure 18a, numerous voids can be observed between crystal particles, suggesting incomplete filling by the liquid phase during ceramic material sintering and consequently low densification of the sintered billet. However, an increased amount of liquid phase generated during sintering can effectively fill these voids within ceramic crystals, leading to

improved ceramics densification [36], as depicted in Figure 18d. Nevertheless, excessive SS content results in an overabundance of liquid phase, which may cause material deformation due to inadequate support for high-temperature creep by particles. Excessive liquid also promotes secondary recrystallization and the abnormal growth of individual grains while inducing stress at grain boundaries, thereby compromising mechanical properties [37].

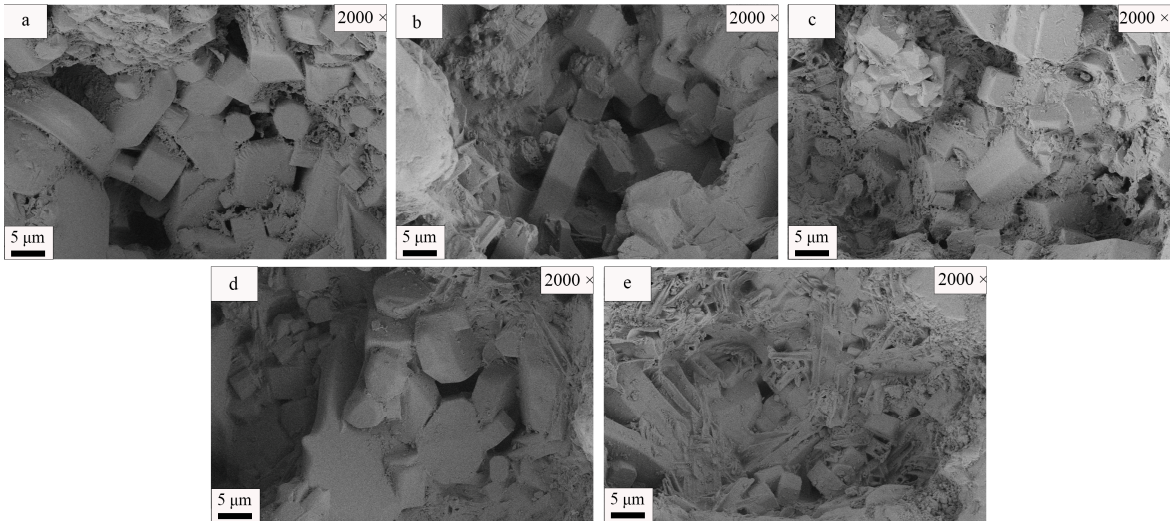

Figure 18. SEM images of samples at 2000× magnification under different SS conditions: (**a**) YG-1; (**b**) YG-2; (**c**) YG-3; (**d**) YG-4; (**e**) YG-5.

The SEM images in Figures 19 and 20 depict ceramic tile samples with varying WCB content at different magnifications. The results indicate that as the WCB content increases, the surface pore size of the sample gradually decreases and then increases. Initially, the average pore size is 79 μm, which reduces to 35.6 μm at a WCB content of 35% but subsequently rises to 54.9 μm at a WCB content of 50%. Furthermore, Figure 19 reveals that when the WCB content increases from 30% to 35%, surface pores transition from a few interconnected pores with diameters greater than 90 μm to numerous tiny pores with diameters less than 50 μm; as the WCB content continues to increase, these pores transform into several interconnected porosity loops with larger diameters.

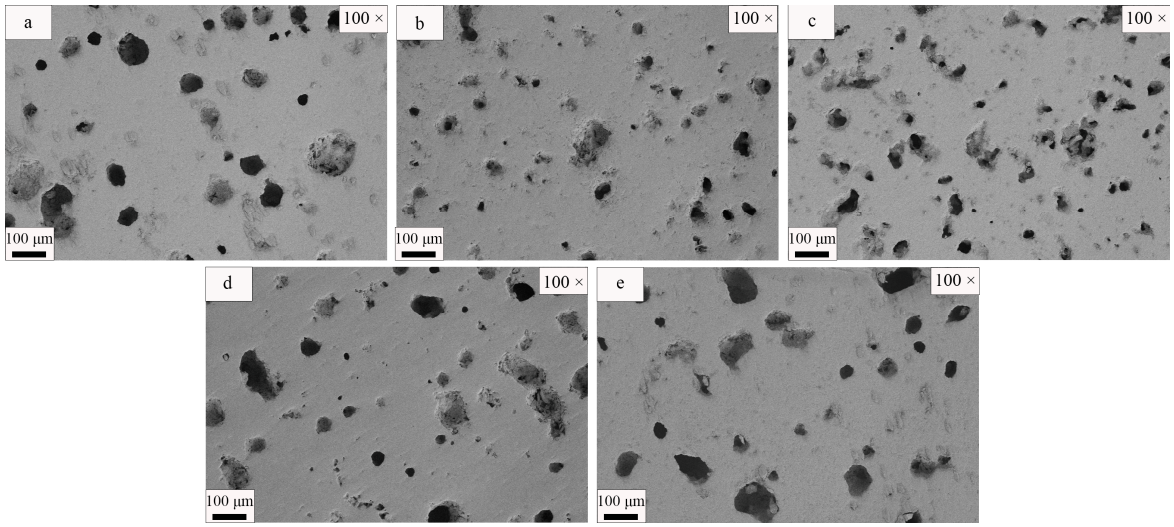

Figure 19. SEM images of samples at 100× magnification under different WCB conditions: (**a**) YZ-1; (**b**) YZ-2; (**c**) YZ-3; (**d**) YZ-4; (**e**) YZ-5.

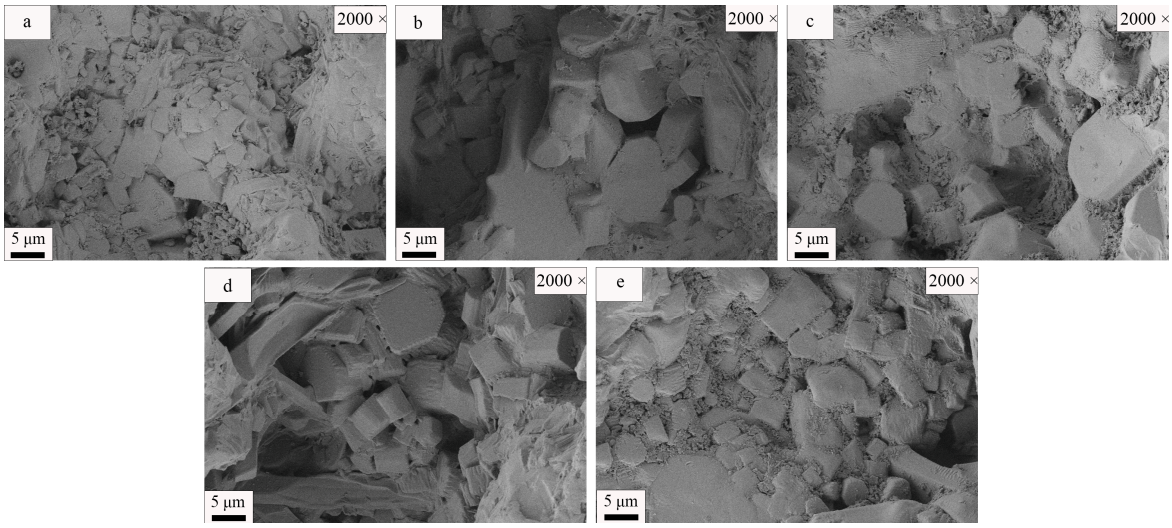

Figure 20. SEM images of samples at 2000× magnification under different WCB conditions: (**a**) YZ-1; (**b**) YZ-2; (**c**) YZ-3; (**d**) YZ-4; (**e**) YZ-5.

Additionally, Figure 20 demonstrates that changes in grain composition within the sample align with XRD diffraction patterns. With increasing WCB content, there is a gradual decrease in hexagonal cylinder crystals, plate crystals, and rhombohedral hexahedral crystals on the bottom of the ceramic sample, while irregular quadrilateral cylinder crystals become more prevalent.

Moreover, Figure 20 also illustrates a gradual decrease in the internal density of the ceramic sample as its WCB content increases. In Figure 20a, it can be observed that grain particles are closely connected through glass phase material, indicating the complete filling of internal grain spaces by liquid phase ceramic material at high temperatures. This results in high-density ceramic bodies formation rate declines due to higher proportions of introduced WCB, leading to incomplete filling into crystal structures and causing an overall decline in density for ceramic bricks, observable in Figure 20b.

The influence of different talc contents on the morphological characteristics of the samples is shown in Figures 21 and 22 at magnifications of 100× and 2000×, respectively. The results indicate that when the talc content is below 30%, the surface of the sample mainly consists of non-connected large pores. As the talc content increases, pore size gradually decreases and then starts to increase. The average pore diameter decreases from 44.63 μm at a content of 20% to 35.01 μm at a content of 25%, and then gradually rises to 38.12 μm at a content of 30%. However, after reaching a talc content above 35%, numerous interconnected small pores appear on the surface, resulting in roughness and unevenness. This phenomenon becomes more pronounced with further increases in talc content.

Furthermore, Figure 22 shows that as the talc content increases, there is an increasing relative proportion of hexagonal columnar crystals and layered crystals on the bottom surface inside the ceramic sample, while irregular quadrilateral columnar crystals decrease gradually. Although there are very few rhombic dodecahedron crystals present, their quantity remains almost unchanged. In addition, Figure 22 also demonstrates that with increasing talc content, both crystal quantity and size within the ceramic material gradually decrease. In Figure 22a–c, it can be observed that grain boundaries are tightly connected by the glass phase between crystal particles, indicating the complete filling of liquid phase into intergranular voids during high-temperature processing, resulting in higher density for ceramic green bodies; however, with higher proportions of introduced talc (as shown in Figure 22c,d), the internal structure becomes looser with a reduced number of grains and decreasing amount of glass phase filling intergranular gaps, which suggests incomplete sintering for ceramic materials at this stage.

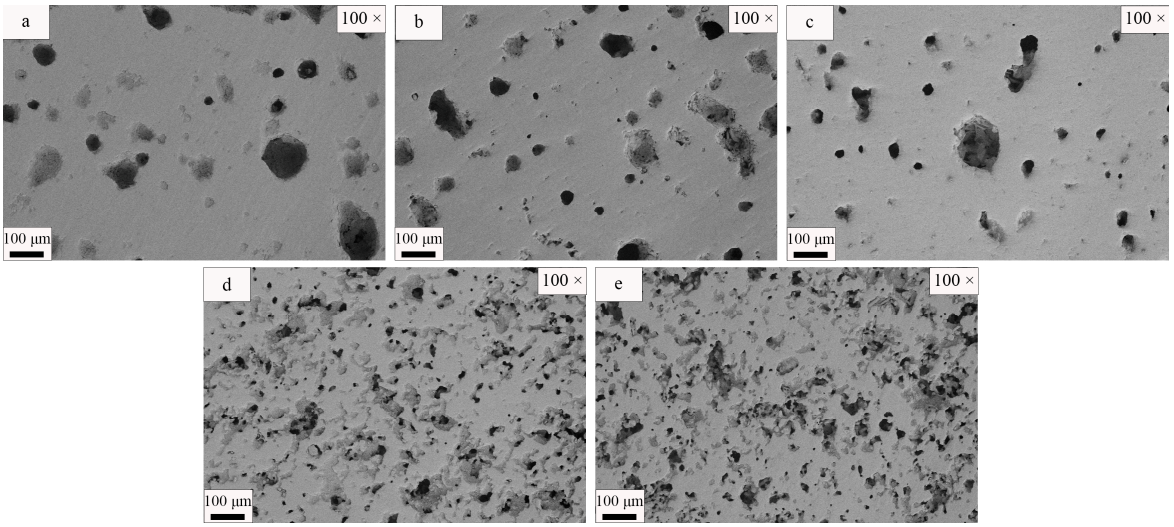

Figure 21. SEM images of samples at 100× magnification under different talc conditions: (**a**) YH-1; (**b**) YH-2; (**c**) YH-3; (**d**) YH-4; (**e**) YH-5.

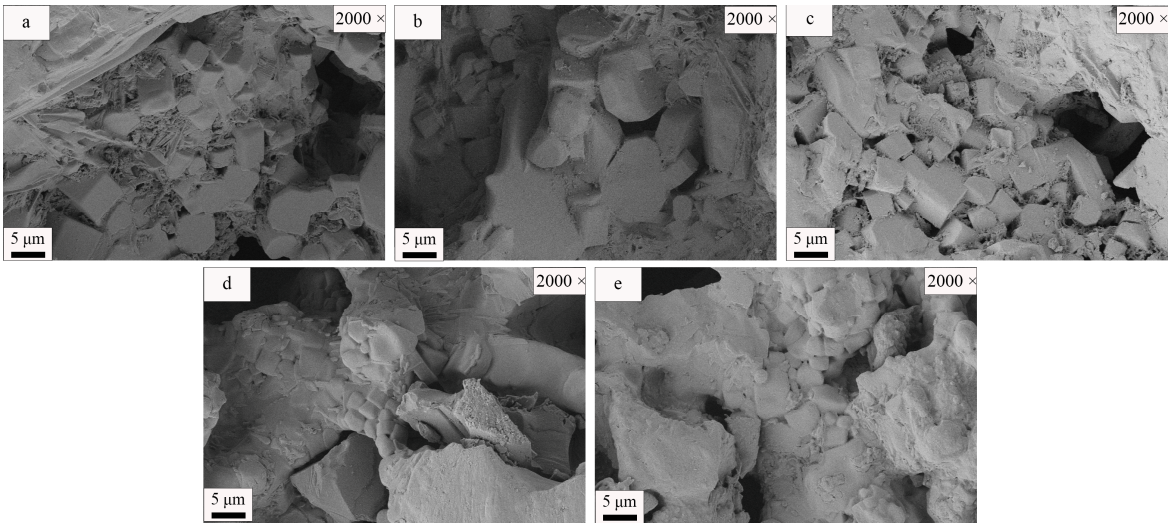

Figure 22. SEM images of samples at 2000× magnification under different talc conditions: (**a**) YH-1; (**b**) YH-2; (**c**) YH-3; (**d**) YH-4; (**e**) YH-5.

3.4. Economic Analysis

The market prices of raw materials for ceramic production in China in 2024 are presented in Table 13, while Table 14 illustrates the proportions of traditional ceramic brick production raw materials and the group of raw materials with optimal performance for ceramic bricks in this experiment. Based on Tables 13 and 14, it can be deduced that the cost of traditional ceramic materials amounts to CNY 1040 per metric ton, whereas the price per metric ton for the experimental formula is merely CNY 285. If this experimental formula is employed for ceramic brick production, a significant reduction of approximately 72.6% can be achieved in terms of raw material costs.

Table 13. The price of raw materials for ceramic production.

Materials	Porcelain Clay	Porcelain Stone	Quartz	Talc	SS	WCB
Price (CNY/ton)	1000	1500	450	950	0	0

Table 14. Proportions of raw materials utilized in ceramic production.

	Porcelain Clay (%)	Porcelain Stone (%)	Quartz (%)	SS (%)	WCB (%)	Talc (%)
Traditional ceramic tile	70	20	10	-	-	-
Ceramic tiles in this experiment	-	-	-	41	36	23

4. Discussion

The experimental results demonstrate a non-linear relationship between the water absorption rate of ceramic tiles and the SS content, which initially decreases and then increases. This can be attributed to the incorporation of SS leading to an increase in the liquid phase, thereby enhancing the densification degree of ceramic materials. These findings are well supported by the results presented in Figures 17 and 18. Additionally, it is observed that the modulus of rupture of ceramic samples decreases with increasing SS content. This phenomenon may arise from variations in both the relative content of main crystal phases within the ceramic brick and the overall densification degree. Analysis results from Table 12 and Figure 18 suggest that at low SS contents, the internal densification of ceramics is relatively poor, with strength primarily governed by internal pyroxene crystals during this stage. As SS content increases further, diopside content decreases while akermanite content increases. Although akermanite exhibits lower crystal phase strength compared to diopside, increased liquid phase production leads to enhanced ceramic densification and the closer arrangement of crystals. Consequently, internal strength predominantly relies on ceramic densification at this stage [38]. However, excessive liquid phase due to higher SS contents causes deformation within the ceramic tile particles, resulting in a decline in water absorption rate and modulus of rupture.

With the increase in WCB content, the water absorption rate of ceramics initially exhibits a significant decrease followed by a slight increase within a narrow range. This phenomenon can be attributed to the relatively high concentration of alkali metal elements in the ceramic body at low WCB content, resulting in excessive liquid phase formation during sintering and leading to the over burning of ceramic tiles [39]. Consequently, this results in higher water absorption rates and lower fracture modules. Figure 19 effectively illustrates this point. Subsequently, as the WCB content increases further, the occurrence of over burning diminishes, causing an increase in both water absorption rate and modulus of rupture for ceramic tiles. However, with a continued rise in WCB content, there is a reduction in liquid phase generation at high temperatures, which subsequently slightly lowers the density of ceramics and leads to a minor increase in water absorption rate along with a decrease in modulus of rupture.

With the increase in talc content, the modulus of rupture of ceramic samples shows a slight initial increase followed by a sharp decrease. This variation can be attributed to the relative content and density of the main crystal phases present in ceramic tiles. As shown in Figure 20, ceramics with lower talc contents experience excessive sintering, leading to a decline in mechanical properties. Subsequently, as the talc content increases, excessive sintering decreases, and overall mechanical properties improve. However, when the talc content is further increased to 27%, both internal density and diopside content slightly decrease, resulting in a minor reduction in strength for ceramic samples. Nevertheless, as the talc content continues to rise to 31%, it becomes evident from Figures 21 and 22 that ceramics no longer achieve complete sintering; porosity increases while internal densification decreases; structure becomes more porous; and the formation of internal crystals also significantly reduces; consequently, a drastic drop occurs in modulus of rupture for this particular ceramic sample. Although both talc and waste clay bricks primarily consist of silicates as raw materials, even when waste clay brick dosage is increased up to 50%, an inadequate sintering phenomenon is not observed for ceramic materials. This may be attributed to waste clay bricks containing flux material such as sodium feldspar, which lowers the sintering temperature for ceramics [40]. However, such additives are absent

in talc, which makes it challenging for ceramics to undergo effective high-temperature sintering after incorporating large amounts of talc [41].

The primary cost structure of traditional ceramic tiles includes expenses for raw materials, labor costs, energy consumption, and other miscellaneous expenditures such as transportation, packaging, and storage. Raw material costs account for approximately one-third of the total tile cost, while labor costs make up around one-fourth to one-third. Currently, energy expenses represent about one-fifth of the overall expenditure, with other costs accounting for roughly one-tenth to one-twentieth. Given that the solid waste materials used in this experiment are challenging-to-handle industrial waste products, their acquisition cost can be disregarded. If the formula derived from this experiment is employed for ceramic tile production purposes, it would result in a significant reduction of 72.6% in raw material expenses. Consequently, this would lead to an approximate 24.2% decrease in total incurred costs. Furthermore, since the sintering temperature required for these experimental ceramic tiles is only 1190 °C—lower than that used in traditional ceramics—it also has the potential to reduce energy consumption during ceramic production.

5. Conclusions

The ceramic material achieved optimal performance when the SS content remained unchanged and the WCB and talc contents were increased to 45%. In this case, the modulus of rupture reached 73.01 MPa, and the water absorption rate was reduced to 0.037%. Similarly, by keeping the SS and talc contents constant while increasing the WCB content to 40%, a ceramic material with improved performance was obtained, exhibiting a modulus of rupture of 82.17 MPa and a water absorption rate of 0.071%. Furthermore, without altering the SS and WCB contents, incorporating 25% talcum resulted in a ceramic material with superior properties, including a modulus of rupture of 73.01 MPa and a water absorption rate of 0.037%.

The addition of SS facilitated an increased liquid phase formation during the sintering process, effectively filling micropores within the ceramic material structure and enhancing its overall performance characteristics. However, the excessive incorporation of SS led to an overabundance of liquid phase, which caused over burning effects on mechanical properties due to excessive heating exposure.

Additionally, higher levels of SS content induced transformation from the diopside crystal phase to the akermanite phase. While WCB addition reduced liquid phase generation at high temperatures as well as decreased ceramic density due to its fluxing component albite presence, extensive incorporation did not negatively impact sintering quality in general terms.

Moreover, WCB promoted transformation from akermanite back into diopside crystal phases. A small amount of talc proved beneficial in mitigating over burning issues arising from alkali metal elements introduced through SS components; however, excessive talc content resulted in insufficient fluxing components, leading to incomplete sintering at temperature conditions set at 1190 °C. Furthermore, talc inclusion facilitated transformation from the diopside crystal phase into the akermanite phase.

Compared to traditional ceramic tiles, the utilization of the formula in this experiment results in a remarkable reduction in raw material costs, amounting to a decrease of 72.6%. Additionally, the overall cost is reduced by approximately 24.2%.

Author Contributions: Conceptualization—Y.J. and E.L.; methodology—Y.J. and E.L.; validation—E.L.; investigation—E.L.; writing—original draft preparation—E.L.; writing—review and editing—Y.J.; supervision—G.Z., R.W. and Q.S.; project administration—Y.J. and E.L.; funding acquisition—Y.J. All authors have read and agreed to the published version of the manuscript.

Funding: This work was funded by the Key Research and Development Plan of Shaanxi Province (Grant No. 2019TSLGY05-04).

Institutional Review Board Statement: Not applicable.

Informed Consent Statement: Not applicable.

Data Availability Statement: The raw and processed data required to reproduce these results are available upon reasonable request.

Conflicts of Interest: Author Gang Zhu was employed by the company China Building Materials Industry Construction Xi'an Engineering Co., Ltd. The remaining authors declare that the research was conducted in the absence of any commercial or financial relationships that could be construed as a potential conflict of interest.

References

1. Teo, P.T.; Zakaria, S.K.; Sharif, N.M.; Abu Seman, A.; Taib MA, A.; Mohamed, J.J.; Yusoff, M.; Yusoff, A.H.; Mohamad, M.; Ali, A.; et al. Application of General Full Factorial Statistical Experimental Design's Approach for the Development of Sustainable Clay-Based Ceramics Incorporated with Malaysia's Electric Arc Furnace Steel Slag Waste. *Crystals* **2021**, *11*, 442. [CrossRef]
2. Gao, W.H.; Zhou, W.T.; Lyu, X.; Liu, X.; Su, H.L.; Li, C.M.; Wang, H. Comprehensive utilization of steel slag: A review. *Powder Technol.* **2023**, *422*, 118449. [CrossRef]
3. Yüksel, I. A review of steel slag usage in construction industry for sustainable development. *Environ. Dev. Sustain.* **2017**, *19*, 369–384. [CrossRef]
4. Gao, T.M.; Dai, T.; Shen, L.; Jiang, L. Benefits of using steel slag in cement clinker production for environmental conservation and economic revenue generation. *J. Clean Prod.* **2021**, *282*, 124538. [CrossRef]
5. Sas, W.; Gluchowski, A.; Radziemska, M.; Dzieciol, J.; Szymanski, A. Environmental and Geotechnical Assessment of the Steel Slags as a Material for Road Structure. *Materials* **2015**, *8*, 4857–4875. [CrossRef]
6. Tozsin, G.; Yonar, F.; Yucel, O.; Dikbas, A. Utilization possibilities of steel slag as backfill material in coastal structures. *Sci. Rep.* **2023**, *13*, 4318. [CrossRef]
7. Barca, C.; Meyer, D.; Liira, M.; Drissen, P.; Comeau, Y.; Andrès, Y.; Chazarenc, F. Steel slag filters to upgrade phosphorus removal in small wastewater treatment plants: Removal mechanisms and performance. *Ecol. Eng.* **2014**, *68*, 214–222. [CrossRef]
8. Yang, L.Y.; Qian, X.M.; Wang, Z.; Li, Y.; Bai, H.; Li, H. Steel slag as low-cost adsorbent for the removal of phenanthrene and naphthalene. *Adsorpt. Sci. Technol.* **2018**, *36*, 1160–1177. [CrossRef]
9. Ning, D.F.; Liang, Y.C.; Liu, Z.D.; Xiao, J.F.; Duan, A.W. Impacts of Steel-Slag-Based Silicate Fertilizer on Soil Acidity and Silicon Availability and Metals-Immobilization in a Paddy Soil. *PLoS ONE* **2016**, *11*, 0168163. [CrossRef]
10. Han, F.; Yun, S.N.; Zhang, C.; Xu, H.F.; Wang, Z.Q. Steel slag as accelerant in anaerobic digestion for nonhazardous treatment and digestate fertilizer utilization. *Bioresour. Technol.* **2019**, *282*, 331–338. [CrossRef]
11. Jiang, Y.; Ling, T.C.; Shi, C.J.; Pan, S.Y. Characteristics of steel slags and their use in cement and concrete—A review. *Resour. Conserv. Recycl.* **2018**, *136*, 187–197. [CrossRef]
12. Liu, G.; Schollbach, K.; Li, P.P.; Brouwers, H.J.H. Valorization of converter steel slag into eco-friendly ultra-high performance concrete by ambient CO2 pre-treatment. *Constr. Build. Mater.* **2021**, *280*, 122580. [CrossRef]
13. Zhang, Y.; Wu, Y.J.; Yang, X.K.; Li, D.H.; Zhang, X.Y.; Dong, X.; Yao, X.H.; Liu, J.C.; Guo, A.R. High-strength thermal insulating mullite nanofibrous porous ceramics. *J. Eur. Ceram. Soc.* **2020**, *40*, 2090–2096. [CrossRef]
14. Zhao, L.H.; Li, Y.; Zhou, Y.Y.; Cang, D.Q. Preparation of novel ceramics with high CaO content from steel slag. *Mater. Des.* **2014**, *64*, 608–613. [CrossRef]
15. Tabit, K.; Hajjou, H.; Waqif, M.; Saâdi, L. Effect of CaO/SiO_2 ratio on phase transformation and properties of anorthite-based ceramics from coal fly ash and steel slag. *Ceram. Int.* **2020**, *46*, 7550–7558. [CrossRef]
16. Ai, X.B.; Bai, H.; Zhao, L.H.; Cang, D.Q.; Tang, Q. Thermodynamic analysis and formula optimization of steel slag-based ceramic materials by FACTsage software. *Int. J. Miner. Metall. Mater.* **2013**, *20*, 379–385. [CrossRef]
17. Zhang, X.D.; Zheng, C.Z.; Liu, S.P.; Zong, Y.B.; Zhou, Q.F.; Qin, S.C. Preparation of Steel Slag Ceramics with Different MgO/Al_2O_3 Ratios. *Appl. Sci.* **2019**, *9*, 4741. [CrossRef]
18. Al-kroom, H.; Atyia, M.M.; Mahdy, M.G.; Abd Elrahman, M. The Effect of Finely-Grinded Crushed Brick Powder on Physical and Microstructural Characteristics of Lightweight Concrete. *Minerals* **2022**, *12*, 159. [CrossRef]
19. Zhao, Y.S.; Gao, J.M.; Chen, F.; Liu, C.B.; Chen, X.M. Utilization of waste clay bricks as coarse and fine aggregates for the preparation of lightweight aggregate concrete. *J. Clean Prod.* **2018**, *201*, 706–715. [CrossRef]
20. Ge, Z.; Wang, Y.Y.; Sun, R.J.; Wu, X.S.; Guan, Y.H. Influence of ground waste clay brick on properties of fresh and hardened concrete. *Constr. Build. Mater.* **2015**, *98*, 128–136. [CrossRef]
21. Ibrahim, J.; Tihtih, M.; Gömze, L.A. Environmentally-friendly ceramic bricks made from zeolite-poor rock and sawdust. *Constr. Build. Mater.* **2021**, *297*, 123715. [CrossRef]
22. Silva, R.V.; de Brito, J.; Lye, C.Q.; Dhir, R.K. The role of glass waste in the production of ceramic-based products and other applications: A review. *J. Clean Prod.* **2017**, *167*, 346–364. [CrossRef]
23. Peng, L.H.; Qin, S. Sintering Behavior and Technological Properties of Low-Temperature Porcelain Tiles Prepared Using a Lithium Ore and Silica Crucible Waste. *Minerals* **2019**, *9*, 731. [CrossRef]
24. Barreto, E.D.; Stafanato, K.V.; Marvila, M.T.; de Azevedo, A.R.G.; Ali, M.; Pereira, R.M.L.; Monteiro, S.N. Clay Ceramic Waste as Pozzolan Constituent in Cement for Structural Concrete. *Materials* **2021**, *14*, 2917. [CrossRef]

25. Aliabdo, A.A.; Abd-Elmoaty, A.-E.M.; Hassan, H.H. Utilization of crushed clay brick in cellular concrete production. *Alex. Eng. J.* **2014**, *53*, 119–130. [CrossRef]
26. Li, H.B.; Zhang, H.B.; Yan, P.F.; Tong, Y.F.; Yan, C.Y.; Ding, Y.F. Experiment on Size Effect and Fractal Characteristics of Waste Brick and Concrete Recycled Aggregate. *Adv. Mater. Sci. Eng.* **2021**, *2021*, 6097897. [CrossRef]
27. Hu, Z.J.; Shi, T.; Cen, M.Q.; Wang, J.M.; Zhao, X.Y.; Zeng, C.; Zhou, Y.; Fan, Y.J.; Liu, Y.M.; Zhao, Z.F. Research progress on lunar and Martian concrete. *Constr. Build. Mater.* **2022**, *343*, 128117. [CrossRef]
28. Zheng, C.; Lou, C.; Du, G.; Li, X.; Liu, Z.; Li, L. Mechanical properties of recycled concrete with demolished waste concrete aggregate and clay brick aggregate. *Results Phys.* **2018**, *9*, 1317–1322. [CrossRef]
29. Deng, X.; Li, J.; Lu, Z.Y.; Zhang, J.J.; Luo, K.; Hou, L.; Niu, Y.H.; Hu, J.; He, K.W. Recycled mineral admixtures based on recycled clay brick. *J. Build. Eng.* **2023**, *76*, 107193. [CrossRef]
30. Zong, Y.B.; Chen, W.H.; Fan, Y.; Yang, T.L.; Liu, Z.B.; Cang, D.Q. Complementation in the composition of steel slag and red mud for preparation of novel ceramics. *Int. J. Miner. Metall. Mater.* **2018**, *25*, 1010–1017. [CrossRef]
31. *GB/T 3810.3-2016*; Ceramic Tiles—Methods of Test—Part 3: Determination of Water Absorption, Apparent Porosity, Apparent Relative Density and Bulk Density. General Administration of Quality Supervision, Inspection and Quarantine of the People's Republic of China: Beijing, China; Standardization Administration of the People's Republic of China: Beijing, China, 2016; p. 8.
32. *GB/T 3810.4-2016*; Ceramic Tiles—Methods of Test—Part 4: Determination of Modulus of Rupture and Failure Strength. General Administration of Quality Supervision, Inspection and Quarantine of the People's Republic of China: Beijing, China; Standardization Administration of the People's Republic of China: Beijing, China, 2016; p. 12.
33. Zhao, L.H.; Li, Y.; Zhang, L.L.; Cang, D.Q. Effects of CaO and Fe_2O_3 on the Microstructure and Mechanical Properties of SiO_2-CaO-MgO-Fe_2O_3Ceramics from Steel Slag. *ISIJ Int.* **2017**, *57*, 15–22. [CrossRef]
34. Ismail, H.; Ahmad, A.; Mohamad, H. Characteristics of akermanite-gehlenite and diopside bioceramics derived from CaO-MgO-Al_2O_3-SiO_2 system as a potential bone substitute material. *J. Aust. Ceram. Soc.* **2023**, *59*, 1361–1371. [CrossRef]
35. Yu, J.W.; Han, Y.X.; Li, Y.J.; Gao, P. Growth behavior of the magnetite phase in the reduction of hematite via a fluidized bed. *Int. J. Miner. Metall. Mater.* **2019**, *26*, 1231–1238. [CrossRef]
36. Dunce, M.; Birks, E.; Antonova, M.; Bikse, L.; Dutkevica, S.; Freimanis, O.; Livins, M.; Eglite, L.; Smits, K.; Sternberg, A. Influence of sintering temperature on microstructure of $Na_{0.5}Bi_{0.5}TiO_3$ ceramics. *J. Alloys Compd.* **2021**, *884*, 160955. [CrossRef]
37. Fisher, J.G.; Kang, S.J.L. Strategies and practices for suppressing abnormal grain growth during liquid phase sintering. *J. Am. Ceram. Soc.* **2019**, *102*, 717–735. [CrossRef]
38. Nakano, M.; Okazaki, J. Ideal Behavior of Sinter Block Densification and Relation Thereof to Yield and Strength in Iron Ore Sintering. *ISIJ Int.* **2011**, *51*, 1418–1424. [CrossRef]
39. Wang, S.; Guo, Y.F.; Liu, K.; Yang, Z.; Liu, Y.J.; Jiang, Y.; Chen, F.; Zheng, F.Q.; Yang, L.Z. The Deposit Formation Mechanism in Coal-Fired Rotary Kiln for Iron Ore Pellet Production: A Review. *Crystals* **2021**, *11*, 974. [CrossRef]
40. Stempkowska, A. Silicate Mineral Eutectics with Special Reference to Lithium. *Materials* **2021**, *14*, 4334. [CrossRef]
41. Lu, J.S.; Li, Y.D.; Zou, C.M.; Liu, Z.Y.; Wang, C.L. Effect of sintering additives on the densification, crystallization and flexural strength of sintered glass-ceramics from waste granite powder. *Mater. Chem. Phys.* **2018**, *216*, 1–7. [CrossRef]